Microstructural and mechanical characterisation of Fe-14Cr-0.22Hf alloy fabricated by spark plasma sintering

M. A. Auger[a]*, Y. Huang[b], H. Zhang[c], C.A. Jones[a], Z. Hong[a], M.P. Moody[a], S.G. Roberts[a, d], P. S. Grant[a]

[a]Department of Materials. University of Oxford. OX1 3PH Oxford, UK.

[b]Hefei University of Technology. Hefei, Anhui, 230009, China

[c]Department of Materials, Loughborough University, Leicestershire, LE11 3TU, UK

[d]Culham Centre for Fusion Energy, Abingdon, Oxon, OX14 3EA, UK.

*Corresponding Author. Address: Department of Materials. University of Oxford. Parks Road. OX1 3PH Oxford, UK. Tel.: +44 (0) 1865 273694. Fax: +44 (0) 1865 273789.

e-mail address: maria.auger@materials.ox.ac.uk (M. A. Auger)

Abstract

Fe-14Cr pre-alloyed powder and pure Hf powder were mechanically alloyed to produce powder with nominal composition Fe-14Cr-0.22Hf (wt. %) that was consolidated by the spark plasma sintering (SPS) technique in order to investigate the ability of Hf to produce a nanometric dispersion of oxide particles in a ferritic matrix. Comprehensive microstructural and mechanical characterisation of the as-milled powder and the consolidated material was performed using electron microscopy, X-ray diffraction, atom probe tomography and indentation techniques. It was shown that Hf additions can effectively produce, by internal oxidation, a fine scale dispersion of Hf-O nanoparticles in the consolidated material. A uniform grain structure was produced in the alloy. Although the nanoparticle dispersion was not homogeneous at the finest scale, the resulting dispersion strengthening contributed

significantly to the hardness. According to these results, internal oxidation of reactive elements rather than direct addition of oxides may offer additional opportunities in the design and development of oxide dispersion strengthened steels.

Keywords: Powder metallurgy; hafnium; ODS steels; SPS; TEM; APT

Introduction

In the development of advanced materials for fission and fusion applications, oxide dispersion strengthened (ODS) steels are amongst the most promising structural materials [1-4]. Their microstructural stability under conditions of high temperature and high stress, resistance to radiation damage and creep resistance, have been extensively demonstrated [5-9]. This performance derives from a homogeneous dispersion of stable nanoparticles in the steel matrix that prevents dislocation motion and grain boundary sliding at high temperature [10]. These nanoparticles can also act as sinks for point defects and He bubbles under irradiation conditions in a nuclear reactor environment [11, 12], which underpins their excellent radiation resistance.

The manufacturing of ODS steels has been widely studied, with different combinations of processing routes investigated. The most common manufacturing approach usually starts with mechanical alloying of elemental or pre-alloyed powders with a low fraction of oxide particles (typically Y_2O_3) with the aim of providing a homogeneous dispersion of oxide nanoparticles in the final consolidated material [13-19]. The use of the spark plasma sintering (SPS) technique [20] to achieve the final densification of the milled powder, has increased in the last years, as it significantly shortens the time required for consolidation to a few minutes, compared with the several hours required for other sintering techniques such as hot isostatic

pressing (HIP). In SPS, high current (1000 – 5000 A) and low voltage (<10 V) DC pulses and a uniaxial pressure (up to 100 MPa) are applied to a powder constrained in a graphite mould, which is heated at a high rate (up to 2000 °C/min) towards a target holding temperature. Isothermal holding times are typically 3 – 20 min and, as the current flow stops, the system rapidly cools down. A wide range of alloys, including TaC [21], transparent Y_2O_3 [22], Ni [23], Al_2O_3 [23], Ti-6Al-4V [24] or W-Ni-Fe [25], have been successfully consolidated by SPS. The effectiveness of this technique in the manufacture of ODS alloys has also been confirmed [26-29].

Hafnium has diverse potential uses in nuclear power reactors, such as thermal neutron absorber in nuclear energy control rods or as a specialized refractory material in elemental form or as hafnium oxide [30]. There are only limited reports of the production and characterization of Fe-Cr-Hf powder so far, but the effectiveness of Hf additions in promoting a dispersion of nanoparticles in mechanically alloyed and annealed powder has been suggested [31-33]. A recent study [34] has also reported effective irradiation resistance enhancement of a Fe-Cr-2Hf (wt.%), cold compressed after mechanical alloying and powder annealing, under 200 keV He irradiation at 500 °C by reducing void swelling, which is significant for potential nuclear uses of this alloy type. In this work, Hf powder was added to Fe-14Cr (wt. %) pre-alloyed powder in order to evaluate its capacity to form a fine dispersion of nanoparticles in a ferritic alloy matrix and to consider the resulting performance with respect to more conventional ODS steels that typically contain Y_2O_3 [15, 16, 35]. A 0.22 wt. % concentration of Hf in the alloy was selected to produce a final oxide fraction comparable with the $0.25Y_2O_3$ (wt. %) content in ODS alloys previously prepared and characterised by authors of the current work [28, 36]. Addition of Hf to steel alloys already containing Y_2O_3 has been shown to promote the formation of finer oxides with respect to the original ODS

alloy [37]. In this work, the effectiveness of Hf addition in promoting a nanometric dispersion of precipitates in a Fe-14Cr (wt. %) alloy was compared with the widely studied use of direct Y_2O_3 additions.

Materials and Methods

Argon-atomised Fe-14Cr (wt. %) pre-alloyed powder (< 150 μm in diameter, Aubert & Duval, France; composition details in Table I) and elemental Hf powder (-325 mesh, 99.6% pure, Alfa Aesar, UK, product number 10201) were used as starting materials to produce mechanically alloyed powder with nominal composition Fe-14Cr-0.22Hf (wt. %) (referred to as 14Hf hereafter). The powder mixture was mechanically alloyed in a planetary ball mill (Fritsch Pulverisette 6) for 60 h at 150 rpm in Ar atmosphere. AISI 52100 steel balls were used in the milling process at a ball-to powder ratio of 10:1. The grinding media were contained in a 500 ml chrome-steel bowl. The milled powder was loaded into a graphite mould lined with graphite paper in an Ar-filled glove box for SPS consolidation.

The SPS process was performed at FCT Systeme GmbH (Rauenstein, Germany) using a uniaxial pressure of 50 MPa for 5 min. The hold temperature of 1150^{o}C was reached at a heating rate of 100^{o}C/min to produce a consolidated disk of ~ 20 mm diam. × 5 mm thick. Further details of the SPS process can be found in [28].

The milled powder was characterised by scanning electron microscopy (SEM), energy dispersive X-ray spectroscopy (EDS), X-ray diffraction (XRD), nanoindentation and atom probe tomography (APT) techniques. The powder sample was prepared for characterisation by embedding it in a conductive phenolic resin and polishing with SiC paper and colloidal silica suspension. The consolidated sample was characterised by SEM, EDS, synchrotron X-ray diffraction, electron back-scattered diffraction (EBSD), Vickers hardness measurements,

transmission electron microscopy (TEM) and APT. Different samples from the consolidated disk were cut, ground and polished with SiC paper and colloidal silica suspension (0.06 μm in size) for direct characterisation or for further TEM and APT sample preparation.

Microstructure and compositional imaging was performed in a JEOL JSM5510 scanning electron microscope equipped with an Oxford Instruments silicon drift detector (SDD). AZtec EDS analysis software was used for data processing. Standard θ-2θ X-ray diffraction measurements were obtained in a Philips PW1710 diffractometer, using Cu Kα wavelength radiation (E = 8.048 keV) at a voltage of 35 kV and a current of 50 mA. The scans were registered in the range $2\theta = 20^{o} – 120^{o}$ in continuous mode using a step size of 0.02^{o} and a scan step time of 1.25 s.

14Hf consolidated by SPS was mounted on an alumina holder and scanned by synchrotron X-ray diffractometry on beamline I11 with a wavelength of 82.5770 pm at the Diamond Light Source (Harwell Science and Innovation Campus, Didcot, UK). EBSD was conducted in a JEOL JSM6500F SEM operated at 20 kV using a probe current of ~ 10 nA; areas of 8 × 12.5 μm^2 were mapped in a square array with a step size of 0.1 μm. TEM was conducted in a JEOL 2100 equipped with STEM-EDS operating at 200 kV and in a JEOL 3000F operating at 300 kV. Samples suitable for TEM observation were prepared by the FIB lift-out technique combined with flash-polishing [36].

APT analysis was carried out in a CAMECA Instruments LEAP® 3000X-HR operating in laser pulsing mode. The specimen base temperature was around 50 K and the laser energy was 0.4 nJ at a repetition rate of 200 kHz. CAMECA IVAS® 3.6.12 commercial software was used for data analysis and reconstruction. Samples suitable for APT characterisation, i. e.

needle shaped with an end radius < 100 nm, were prepared following two preparation routes: FIB lift-out and electropolishing. Samples from the milled powder embedded in phenolic conductive resin were prepared by the FIB lift-out technique [38]. The instrument used for APT and TEM sample preparation by the lift-out method was a Zeiss Auriga 40 FIB/SEM. Small bars with dimensions 0.5 mm ×0.5 mm × 20 mm were cut, ground and polished from the SPS consolidated disks. Each bar was submitted to a standard electropolishing process [39]: first, the specimen was repeatedly dipped into a layer of electrolyte (25 % vol. perchloric acid + 75 % vol. acetic acid) on top of a perfluorinated polyether (PFPE) inert liquid (Galden^{TM} solution). A gold wire was used as counter electrode and a DC voltage of 15 V, gradually reduced to 10 – 8 V, was applied until the bar necked in the immersion region and split in two parts. Each part was refined to the final shape, i. e. having a final radius below 100 nm in the needle apex, by dipping the sample through a gold loop holding a drop of a milder electrolyte (2% vol. perchloric acid + 98% vol. 2-butoxyethanol) and applying a DC voltage of 8 – 4 V.

Nanoindentation measurements were made using a Nanoindenter XP (MTS, TN, USA) with a Berkovich diamond indenter calibrated against fused silica. The measurements were performed at room temperature in continuous stiffness mode, using a 2 nm 45 Hz harmonic displacement and reaching depths up to 2 μm below the sample surface. Hardness measurements were performed at room temperature using a Vickers indenter and a load of 1 kg held for 10 s; 15 independent indentations were made.

Results and discussion

SEM-EDS characterisation

The morphology of the as-milled powder, observed by SEM in Fig. 1-a, shows that the powder particles were disc-shaped, with diameters of 200 to 300 μm and thicknesses between 60 and 100 μm. An EDS spectrum from one of the powder particles displayed in Fig. 1-a is shown in Fig. 1-b with measured concentrations of Fe, Cr and Hf in the as-milled powder that were in good agreement with the nominal alloy composition. There was some very limited Si contamination, most likely linked to the manufacturing process and/or impurities in the as-supplied Fe-14Cr pre-alloyed powder. The surface of the SPS consolidated alloy is displayed in Fig. 2-a, showing some randomly distributed dark particles, sized 1 – 4 μm. The chemical maps shown in Fig. 2-b, performed on the central particle in Fig. 2-a, showed that these dark precipitates were rich in Si, again suggesting Si impurities precipitated during consolidation. These precipitates were present in fractions too low to be detected by either laboratory or synchrotron XRD (see below).

Laboratory XRD characterisation

Laboratory θ-2θ X-ray diffractograms were obtained from the Hf powder used in the milling process and from the as-milled 14Hf powder. Fig. 3-a shows that the Hf powder was hexagonal, in accordance with the 638559 file in the FIZ Karlsruhe-ICSD database [40]. Two extra diffraction peaks were assigned to the phenolic resin in which the milled powder was embedded, confirmed by a resin-only diffraction measurement. Fig. 3-b shows the diffractogram from the as-milled 14Hf powder. No distinct, resolvable Hf peaks were present, implying that the Hf powder may have completely dissolved in the Fe-Cr matrix after the mechanical alloying process, producing a single BCC ferrite solid solution.

Synchrotron X-ray diffraction

The synchrotron X-ray diffractogram obtained from 14Hf consolidated by SPS is shown in Fig. 4. Fig. 4-a shows the full synchrotron XRD pattern with both ferrite and austenite phases. Although Fe-14Cr (wt.%) would not usually form austenite at any temperature, based on the Fe-Cr phase diagram [41], Hf may act as an austenite stabilizer according to the Fe-Hf phase diagram [41]. Austenite formed during the 1150^{o}C high temperature SPS process was retained at room temperature due to the rapid cooling after consolidation. Fig. 4-b shows a zoomed-in count region from Fig. 4-a with orthorhombic and monoclinic HfO_2 phases resolved, agreeing with 79913 [42] and 27313 [43] files respectively in the FIZ Karlsruhe-ICSD database. An overlap with $Cr_{23}C_6$ (JCPDS file number 035-0783) and Cr_2O_3 (JCPDS file number 38-1479) was also resolved. The Al_2O_3 peaks were associated with the sample holder used in the experiment.

EBSD

Fig. 5 shows an EBSD grain orientation map as an inverse pole figure (IPF) from the 14Hf alloy consolidated by SPS. High angle grain boundaries were defined as being those having a misorientation higher than 5^{o}; sub-grain boundaries were defined as having a misorientation between 0^{o} and 5^{o}. Most grains in the alloy were ferritic, with random grain orientation and a grain size in the range 0.5 μm to 8 μm, with some occasional larger grains. The temperature used in the SPS process was ~0.76T_m [41] of the Fe-14Cr alloy, where the growth of larger grains might be expected, so the presence of Hf may have conferred thermal stability to the microstructure. For comparison, two alloys with nominal composition Fe-14Cr-0.4Ti-0.25Y_2O_3 (wt.%) and Fe-14Cr-0.25Y_2O_3-0.22Hf (wt.%), mechanically alloyed and SPS consolidated under the same conditions, showed grain sizes up to 15 μm. [28, 36].

TEM characterisation

A general view of the microstructure of the 14Hf alloy consolidated by SPS at high magnification is shown in Fig. 6-a, with precipitates along grain boundaries. The grain microstructure was considerably uniform, with most grains in the range 1 to 5 μm in size. As the atomic number of Hf (Z=72) is much higher than those of Fe (Z=26) and Cr (Z=24), any second-phase precipitates should be relatively easy to resolve by high-angle annular dark-field (HAADF) imaging. Fig. 6-b shows dispersoids with brighter contrast than the matrix, arising from a higher average atomic number (Z) and/or higher average density when compared with the Fe-Cr matrix. To confirm the chemical composition of the dispersoids, EDS mapping was performed and Fig. 7 shows a dispersoid enriched in Hf and O on a grain boundary. HR-TEM was used to investigate similar dispersoids in the matrix, but it was not possible to reliably index the resulting diffraction patterns, for which a contributory factor may be due to non-stoichiometric HfO_x.

A total of 1119 particles were counted and measured from 26 micrographs taken at 5 different regions of the sample, including grain centres and regions containing grain boundaries, to produce the size distribution displayed in Fig. 8, with a typical dispersoid diameter of 2.0 ± 1.5 nm and a number density of 0.8×10^{23} m^{-3}. Dispersoids of approximately 2 nm size were quite uniformly distributed. There was also a small fraction of larger dispersoids, up to 26 nm in size, mostly found on the grain boundaries where diffusion and coarsening can be expected to be relatively fast, although occasionally some were present in grain centres.

APT characterisation

APT was used to investigate the as-milled 14Hf powder and the consolidated alloy, with datasets consisting of 22 – 24 million ions. The reconstructed ion maps for 14Hf powder are displayed in Fig. 9 and Video 1. A relatively uniform distribution of Hf in the Fe-Cr matrix

was obtained after the alloy milling process. APT revealed a small Cr-O precipitate that might have formed during milling or during subsequent powder handling. Fig. 10 shows reconstructed volumes from different regions in the 14Hf alloy after the SPS consolidation: a volume with no clusters in Fig. 10-a) and Video 2, a volume with 0.83×10^{23} m^{-3} number density of clusters in Fig. 10-b) and Video 3, and a high number density of clusters (2.37×10^{23} m^{-3}) region in Fig. 10-c) and Video 4. The regions with no clusters, low density of clusters and high density of clusters represent 38, 27 and 35%, respectively, of the analysed volume. The maximum separation method was implemented for cluster analysis [44], considering Hf-O and O as ions being at the core of the clusters, with Cr-O ions likely to be surrounding them, according to previous APT reconstruction of similar ODS steels containing Y-rich clusters [45]. The resulting cluster size (in terms of the Guinier diameter, i.e. twice the Guinier radius [46]) distribution from the APT measurements in the regions containing clusters is shown in Fig. 11-a and summarised in Table II. The average distance between each cluster and its first neighbour was also calculated as the distance between their centres of mass [46]; results for the high and low number density of clusters regions are summarised in Table II.

The shape of the clusters can be defined using a best-fit ellipsoid enclosing each individual cluster [47]. The smallest, middle and largest characteristic lengths of the best-fit ellipsoids were used to calculate the oblateness (smallest characteristic length / middle characteristic length) and the aspect ratio (middle characteristic length / largest characteristic length) of the clusters. Combinations of these two parameters can be used to define the cluster shape as sphere, rod, lath or disc. Fig. 11-b displays the oblateness and aspect ratio measurements for the clusters present in 14Hf consolidated by SPS, and the quantification of each cluster shape

is summarised in Table III. The majority of the clusters, in both the regions containing clusters in high and low number density, were spherical.

The chemical composition of each cluster was also analysed by APT. Fig. 12 shows the O:Hf ratio for each individual cluster as a function of the cluster size, with a ratio close to O:Hf = 1 for most of the clusters. An averaged ratio of O:Hf = 1.08 ± 0.07, for values in the range 1 to 1.27 was obtained for the clusters in the high density region, and O:Hf = 0.99 ± 0.02 in a 0.93 to 1.01 range for clusters in the low density region. This demonstrates that there was Hf and O enrichment of the clusters, but not reaching the HfO_2 stoichiometry. Possible Hf-containing precipitates include HfO_2, HfC and Hf-containing intermetallic compounds. The Gibbs free energy for the formation of HfO_2 and HfC at 1150^{o}C are ΔG_f (HfO_2)= −1306 kJ/mol according to [48] and ΔG_f (HfC)= −219 kJ/mol according to [49]. The Gibbs free energy for the formation of intermetallics would be ~ −100 kJ/mol according to [32]. In the present work, due to the 0.22 wt. % Hf concentration, only sub-stoichiometric Hf-O particles have formed. The sub-stoichiometric Hf-O dispersoids were likely responsible for the orthorhombic and monoclinic phases observed in the synchrotron X-ray diffractograms (Fig. 4-b). Also, the dispersoid size being typically < 5 nm, suggests that precipitation occurred during the relatively short (5 min) thermal exposure of the SPS process, but there is little evidence for any significant dispersoid coarsening after initial nucleation.

Hardness measurements

The nanoindentation hardness profile of the as-milled 14Hf powder is shown in Fig. 13-a. Apart from a slight variation associated with the initial penetration of the polished surface of powders, the hardness tends to an approximately constant value of 7.74 ± 0.27 GPa with increasing indentation depth. This comparatively high hardness could be associated with

strain hardening induced during the mechanical alloying process and/or the indentation size effect by which hardness values at sub-μm indentation depths can be 2-3 times those of macroscopic indentations [50]. Vickers hardness measurements were performed on the consolidated 14Hf (Fig. 13-b), with 15 random indentations over the sample surface giving an average 2.31 ± 0.13 GPa, ~ 30% lower than that for a Fe-14Cr-0.3Y_2O_3 (wt. %) alloy consolidated by HIP (hardness = 3.60 ± 0.08 GPa) [27]. The hardness of a Fe-14Cr (wt. %) alloy manufactured by SPS at 1150^{o}C was 1.74 ± 0.04 GPa [27]; this will be taken as a "base value" when assessing effects of possible hardening mechanisms. The difference in hardness between the ODS alloys containing Hf and Y might be due to differences in the contributions to the flow stress of solid solution strengthening, dislocation strengthening, dispersion strengthening and/or fine grain strengthening [31, 51]. It is likely that the contributions from solid solution strengthening contribution are similar in the two alloys, as the matrix is Fe-14Cr (wt. %) in both cases and both Y and Hf are virtually insoluble in the matrix at equilibrium. It may be assumed that dislocation strengthening had a relatively weak effect because no dislocations were observed by TEM (Fig. 6 and [16, 45]).

Regarding grain size strengthening ('Hall-Petch' effect [52]), the 14Hf alloy has a relatively uniform grain size of 1 to 5 μm; Fe-14Cr-0.3Y_2O_3 consolidated by HIP also had a uniform grain structure with slightly smaller grains, in the range 0.5 to 3 μm [16]), significantly contributing to the hardness as shown in Table IV.

The dispersion strengthening contribution, H_O, can be estimated by assuming Orowan strengthening, according to [31, 53]:

$$H_O = 3\sqrt{3}\left(\frac{ln(d/r_0)}{ln(L/r_0)}\right)^{3/2}\frac{Gb}{L}\frac{ln(L/r_0)}{2\pi} \qquad (1)$$

where *d* is the precipitate size (taken as the cluster diameter from APT measurements in Table II), *L* is the interprecipitate spacing (taken as the intercluster distance from APT measurements in Table II), *G* is the shear modulus for Fe (82 GPa), *b* is the Burgers vector

(0.384 nm) and r_0 is the dislocation core radius, assumed to be four times the Burgers vector (1.536 nm). As the dispersion of nanoparticles is not homogeneous, the contributions to Orowan hardening from the regions of high and low number density of clusters has been considered separately taking into account the respective cluster analysis and volumes represented by each region type obtained by APT characterisation. The calculations are detailed in Table V and summarised in Table IV. The most significant contribution to the total hardness in both alloys is Orowan hardening. The Orowan hardening is significantly higher for the Fe-14Cr-0.3Y_2O_3 (wt. %) alloy consolidated by HIP than for 14Hf consolidated by SPS because the cluster number density is higher (3.30×10^{23} m^{-3} [45]), the cluster size is smaller (3.06 ± 0.68 nm [45]) and the clusters are closer together (intercluster distance = 9.87 ± 2.37 nm).

Conclusions

- The effectiveness of elemental Hf addition to a ferritic steel powder to promote a nanometric distribution of clusters in the densified steel has been demonstrated. Elemental Hf dissolved in the Fe-14Cr (wt. %) matrix during the mechanical alloying and then precipitated as Hf-O rich clusters during SPS consolidation. The approach is an alternative to the more common adding of ceramic oxides, such as Y_2O_3, directly to ferritic powders.
- Hf-O dispersoids stabilised a relatively uniform grain structure, with grain sizes between 1 and 5 μm, although Hf-O nanoparticle dispersion was not homogeneous at the finest scale, as both regions with no particles and regions with high and low number density of Hf-O rich precipitates were observed by APT. The cluster size of the precipitates was approximately 2 nm by TEM, with a number density of 0.8×10^{23} m^{-3}. The cluster size measured by APT was 2.34 ± 0.77 nm in the region with a high number density of

clusters (2.37×10^{23} m^{-3}) and 3.64 ± 0.98 nm in the region with a low number density of clusters (0.83×10^{23} m^{-3}).

- After SPS consolidation, Hf was predominantly in the form of Hf-O precipitates, with orthorhombic and monoclinic crystalline structures, with a O:Hf ratio close to 1. No other Hf-rich compounds such as HfC or Fe-Cr-Hf were detected.
- Dispersion strengthening was the primary contribution to the final hardness, consistent with conventional ODS steels using direct oxide additions.

Acknowledgements

The authors acknowledge funding by the UK Engineering and Physical Sciences Research Council (EPSRC) through Grant Numbers EP/H018921/1 and EP/P006566 (MAPP), Diamond Light Source for access to beamline I11 (Proposal No. EE10597) and the use of the EPSRC funded National Chemical Database Service hosted by the Royal Society of Chemistry.

References

[1] G.R. Odette, M.J. Alinger, B.D. Wirth, Recent developments in irradiation-resistant steels, Annu Rev Mater Res 38 (2008) 471-503.
[2] A. Hirata, T. Fujita, Y.R. Wen, J.H. Schneibel, C.T. Liu, M.W. Chen, Atomic structure of nanoclusters in oxide-dispersion-strengthened steels, Nat Mater 10(12) (2011) 922-926.
[3] G.R. Odette, Recent Progress in Developing and Qualifying Nanostructured Ferritic Alloys for Advanced Fission and Fusion Applications, Jom-Us 66(12) (2014) 2427-2441.
[4] R.L. Klueh, J.P. Shingledecker, R.W. Swindeman, D.T. Hoelzer, Oxide dispersion-strengthened steels: A comparison of some commercial and experimental alloys, J Nucl Mater 341(2-3) (2005) 103-114.
[5] P. Pareige, M.K. Miller, R.E. Stoller, D.T. Hoelzer, E. Cadel, B. Radiguet, Stability of nanometer-sized oxide clusters in mechanically-alloyed steel under ion-induced displacement cascade damage conditions, J Nucl Mater 360(2) (2007) 136-142.
[6] T.R. Allen, J. Gan, J.I. Cole, M.K. Miller, J.T. Busby, S. Shutthanandan, S. Thevuthasan, Radiation response of a 9 chromium oxide dispersion strengthened steel to heavy ion irradiation, J Nucl Mater 375(1) (2008) 26-37.
[7] A. Certain, S. Kuchibhatla, V. Shutthanandan, D.T. Hoelzer, T.R. Allen, Radiation stability of nanoclusters in nano-structured oxide dispersion strengthened (ODS) steels, J Nucl Mater 434(1-3) (2013) 311-321.
[8] V. de Castro, S. Lozano-Perez, M. Briceno, P. Trocellier, S.G. Roberts, R. Pareja, Effects of single- and simultaneous triple-ion-beam irradiation on an oxide dispersion-strengthened Fe12Cr steel, J Mater Sci 50(5) (2015) 2306-2317.
[9] T.Y. Chen, E. Aydogan, J.G. Gigax, D. Chen, J. Wang, X.M. Wang, S. Ukai, F.A. Garner, L. Shao, Microstructural changes and void swelling of a 12Cr ODS ferritic-martensitic alloy after high-dpa self-ion irradiation, J Nucl Mater 467 (2015) 42-49.
[10] F. Siska, L. Stratil, H. Hadraba, S. Fintova, I. Kubena, T. Zalezak, D. Bartkova, High temperature deformation mechanisms in the 14% Cr ODS alloy, Materials Science and Engineering: A 689 (2017) 34-39.

[11] M. Šćepanović, V. de Castro, T. Leguey, M.A. Auger, S. Lozano-Perez, R. Pareja, Microstructural stability of ODS Fe–14Cr (–2W–0.3Ti) steels after simultaneous triple irradiation, Nuclear Materials and Energy 9 (2016) 490-495.
[12] C.M. Parish, K.A. Unocic, L. Tan, S.J. Zinkle, S. Kondo, L.L. Snead, D.T. Hoelzer, Y. Katoh, Helium sequestration at nanoparticle-matrix interfaces in helium + heavy ion irradiated nanostructured ferritic alloys, J Nucl Mater 483 (2017) 21-34.
[13] M.J. Alinger, G.R. Odette, D.T. Hoelzer, On the role of alloy composition and processing parameters in nanocluster formation and dispersion strengthening in nanostuctured ferritic alloys, Acta Mater 57(2) (2009) 392-406.
[14] M.A. Auger, T. Leguey, A. Munoz, M.A. Monge, V. de Castro, P. Fernandez, G. Garces, R. Pareja, Microstructure and mechanical properties of ultrafine-grained Fe-14Cr and ODS Fe-14Cr model alloys, J Nucl Mater 417(1-3) (2011) 213-216.
[15] P. He, M. Klimenkov, R. Lindau, A. Moslang, Characterization of precipitates in nano structured 14% Cr ODS alloys for fusion application, J Nucl Mater 428(1-3) (2012) 131-138.
[16] M.A. Auger, V. de Castro, T. Leguey, M.A. Monge, A. Munoz, R. Pareja, Microstructure and tensile properties of oxide dispersion strengthened Fe-14Cr-0.3Y(2)O(3) and Fe-14Cr-2W-0.3Ti-0.3Y(2)O(3), J Nucl Mater 442(1-3) (2013) S142-S147.
[17] Z. Oksiuta, P. Hosemann, S.C. Vogel, N. Baluc, Microstructure examination of Fe-14Cr ODS ferritic steels produced through different processing routes, J Nucl Mater 451(1-3) (2014) 320-327.
[18] D.T. Hoelzer, K.A. Unocic, M.A. Sokolov, T.S. Byun, Influence of processing on the microstructure and mechanical properties of 14YWT, J Nucl Mater 471 (2016) 251-265.
[19] C.C. Eiselt, H. Schendzielorz, A. Seubert, B. Hary, Y. de Carlan, P. Diano, B. Perrin, D. Cedat, ODS-materials for high temperature applications in advanced nuclear systems, Nuclear Materials and Energy 9 (2016) 22-28.
[20] Z.A. Munir, D.V. Quach, M. Ohyanagi, Electric Current Activation of Sintering: A Review of the Pulsed Electric Current Sintering Process, J Am Ceram Soc 94(1) (2011) 1-19.
[21] L.M. Liu, F. Ye, Y. Zhou, New route to densify tantalum carbide at 1400 degrees C by spark plasma sintering, Mat Sci Eng A 528(13-14) (2011) 4710-4714.
[22] L.Q. An, A. Ito, T. Goto, Transparent yttria produced by spark plasma sintering at moderate temperature and pressure profiles, J Eur Ceram Soc 32(5) (2012) 1035-1040.
[23] L. Minier, S. Le Gallet, Y. Grin, F. Bernard, A comparative study of nickel and alumina sintering using spark plasma sintering (SPS), Mater. Chem. Phys. 134(1) (2012) 243-253.
[24] K. Crosby, L.L. Shaw, C. Estournes, G. Chevallier, A.W. Fliflet, M.A. Imam, Enhancement in Ti-6Al-4V sintering via nanostructured powder and spark plasma sintering, Powder Metall. 57(2) (2014) 147-154.
[25] V.N. Chuvildeev, D.V. Panov, M.S. Boldin, A.V. Nokhrin, Y.V. Blagoveshchensky, N.V. Sakharov, S.V. Shotin, D.N. Kotkov, Structure and properties of advanced materials obtained by Spark Plasma Sintering, Acta Astronaut. 109 (2015) 172-176.
[26] C. Heintze, M. Hernandez-Mayoral, A. Ulbricht, F. Bergner, A. Shariq, T. Weissgarber, H. Frielinghaus, Nanoscale characterization of ODS Fe-9%Cr model alloys compacted by spark plasma sintering, J Nucl Mater 428(1-3) (2012) 139-146.
[27] M.A. Auger, V. de Castro, T. Leguey, A. Munoz, R. Pareja, Microstructure and mechanical behavior of ODS and non-ODS Fe-14Cr model alloys produced by spark plasma sintering, J Nucl Mater 436(1-3) (2013) 68-75.
[28] H.T. Zhang, Y.N. Huang, H.P. Ning, C.A. Williams, A.J. London, K. Dawson, Z.L. Hong, M.J. Gorley, C.R.M. Grovenor, G.J. Tatlock, S.G. Roberts, M.J. Reece, H.X. Yan, P.S. Grant, Processing and microstructure characterisation of oxide dispersion strengthened Fe-14Cr-0.4Ti-0.25Y(2)O(3) ferritic steels fabricated by spark plasma sintering, J Nucl Mater 464 (2015) 61-68.
[29] I. Hilger, X. Boulnat, J. Hoffmann, C. Testani, F. Bergner, Y. De Carlan, F. Ferraro, A. Ulbricht, Fabrication and characterization of oxide dispersion strengthened (ODS) 14Cr steels consolidated by means of hot isostatic pressing, hot extrusion and spark plasma sintering, J Nucl Mater 472 (2016) 206-214.
[30] E.M. Harper, Z. Diao, S. Panousi, P. Nuss, M.J. Eckelman, T.E. Graedel, The criticality of four nuclear energy metals, Resources, Conservation and Recycling 95 (2015) 193-201.
[31] L.L. Li, M. Saber, W.Z. Xu, Y.T. Zhu, C.C. Koch, R.O. Scattergood, High-temperature grain size stabilization of nanocrystalline Fe-Cr alloys with Hf additions, Mat Sci Eng A 613 (2014) 289-295.
[32] W.Z. Xu, L.L. Li, M. Saber, C.C. Koch, Y.T. Zhu, R.O. Scattergood, Microstructures and Stabilization Mechanisms of Nanocrystalline Iron-Chromium Alloys with Hafnium Addition, Metall Mater Trans A 46a(9) (2015) 4394-4404.
[33] P.S. Roodposhti, M. Saber, C. Koch, R. Scattergood, S. Shahbazmohamadi, Effect of oxygen content on thermal stability of grain size for nanocrystalline Fe10Cr and Fe14Cr4Hf alloy powders, J Alloy Compd 720 (2017) 510-520.

[34] W.Z. Xu, L.L. Li, J.A. Valdez, M. Saber, Y.T. Zhu, C.C. Koch, R.O. Scattergood, Effect of nano-oxide particle size on radiation resistance of iron-chromium alloys, J Nucl Mater 469 (2016) 72-81.
[35] M.K. Miller, K.F. Russell, D.T. Hoelzer, Characterization of precipitates in MA/ODS ferritic alloys, J Nucl Mater 351(1-3) (2006) 261-268.
[36] Y. Huang, H. Zhang, M.A. Auger, Z. Hong, H. Ning, M.J. Gorley, P.S. Grant, M.J. Reece, H. Yan, S.G. Roberts, Microstructural comparison of effects of hafnium and titanium additions in spark-plasma-sintered Fe-based oxide-dispersion strengthened alloys, J Nucl Mater 487 (2017) 433-442.
[37] H. Oka, M. Watanabe, S. Ohnuki, N. Hashimoto, S. Yamashita, S. Ohtsuka, Effects of milling process and alloying additions on oxide particle dispersion in austenitic stainless steel, J Nucl Mater 447(1-3) (2014) 248-253.
[38] M.K. Miller, K.F. Russell, Atom probe specimen preparation with a dual beam SEM/FIB miller, Ultramicroscopy 107(9) (2007) 761-766.
[39] B. Gault, Atom probe microscopy, Springer, New York, 2012.
[40] R.B. Russell, On the Zr-Hf System, J Appl Phys 24(2) (1953) 232-233.
[41] W.G. Moffatt, General Electric Company., The handbook of binary phase diagrams, General Electric Co, Schenectady, 1978.
[42] O. Ohtaka, T. Yamanaka, S. Kume, N. Hara, H. Asano, F. Izumi, Structural-analysis of orthorhombic hafnia by neutron powder diffraction, J Am Ceram Soc 78(1) (1995) 233-237.
[43] R. Ruh, P.W. Corfield, Crystal Structure of Monoclinic Hafnia and Comparison with Monoclinic Zirconia, J Am Ceram Soc 53(3) (1970) 126-+.
[44] M.K. Miller, Atom probe tomography : analysis at the atomic level, Kluwer Academic/Plenum Publishers, New York ; London, 2000.
[45] M.A. Auger, V. de Castro, T. Leguey, S. Lozano-Perez, P.A.J. Bagot, M.P. Moody, S.G. Roberts, Effect of the milling atmosphere on the microstructure and mechanical properties of a ODS Fe-14Cr model alloy, Mat Sci Eng A 671 (2016) 264-274.
[46] M.K. Miller, E.A. Kenik, Atom probe tomography: A technique for nanoscale characterization, Microsc Microanal 10(3) (2004) 336-341.
[47] R.K.W. Marceau, L.T. Stephenson, C.R. Hutchinson, S.P. Ringer, Quantitative atom probe analysis of nanostructure containing clusters and precipitates with multiple length scales, Ultramicroscopy 111(6) (2011) 738-742.
[48] M.C. Zeman, C.C. Fulton, G. Lucovsky, R.J. Nemanich, W.C. Yang, Thermal stability of TiO2, ZrO2, or HfO2 on Si(100) by photoelectron emission microscopy, J Appl Phys 99(2) (2006).
[49] Y.C. Ye, H. Zhang, Y.G. Tong, S.X. Bai, HfC-based coating prepared by reactive melt infiltration on C/C composite substrate, Ceram Int 39(5) (2013) 5477-5483.
[50] W.D. Nix, H.J. Gao, Indentation size effects in crystalline materials: A law for strain gradient plasticity, J Mech Phys Solids 46(3) (1998) 411-425.
[51] X.D. Mao, S.H. Kang, T.K. Kim, S.C. Kim, K.H. Oh, J. Jang, Microstructure and Mechanical Properties of Ultrafine-Grained Austenitic Oxide Dispersion Strengthened Steel, Metall Mater Trans A 47a(11) (2016) 5334-5343.
[52] X.D. Liu, M. Nagumo, M. Umemoto, The Hall-Petch Relationship in Nanocrystalline Materials, Materials Transactions, JIM 38(12) (1997) 1033-1039.
[53] D.J. Bacon, U.F. Kocks, R.O. Scattergood, The effect of dislocation self-interaction on the orowan stress, Philosophical Magazine 28(6) (1973) 1241-1263.

Table captions

Table I. Chemical composition of the Fe-14Cr (wt. %) pre-alloyed powder.

Table II. Summary of the cluster size, intercluster distance and number density of clusters in the 14Hf alloy consolidated by SPS in the low and high cluster density regions.

Table III. Summary of the cluster shape in the regions with low and high number density of clusters in the14Hf alloy consolidated by SPS.

Table IV. Summary of hardness, total hardening, Orowan and Hall-Petch contributions to the total hardening for the 14Hf alloy consolidated by SPS and Fe-14Cr-0.3Y_2O_3 (wt.%) alloy consolidated by HIP [27, 45]. Hardness of Fe-14Cr consolidated by SPS is shown as the reference value [27].

Table V. Orowan hardness calculations for the 14Hf alloy consolidated by SPS considering the different cluster density regions observed by APT.

Figure captions

Fig. 1. a) SEM image of as-milled 14Hf powder. b) EDS quantification of one 14Hf powder particle.

Fig. 2 a) SEM image of 14Hf alloy consolidated by SPS. b) SEM image, mapping and EDS analysis of Fe, Cr and Si of one dark particle in the 14Hf alloy consolidated by SPS.

Fig. 3. X-ray diffraction patterns of a) elemental Hf powder and b) as-milled 14Hf powder highlighting the phases present.

Fig. 4. Synchrotron X-ray diffraction patterns of 14Hf alloy consolidated by SPS. a) Overview of the pattern. b) zoomed-in pattern to show minor phases.

Fig. 5. EBSD inverse pole figure (IPF) map of 14Hf alloy consolidated by SPS. Grain orientations are colour-coded according to the inset standard triangle.

Fig. 6. a) Bright field TEM and b) HAADF images of 14Hf alloy consolidated by SPS.

Fig. 7. STEM DF image and EDS mapping of Fe, Cr, Hf and O in 14Hf alloy consolidated by SPS.

Fig. 8. Size distribution of the nanoparticles from TEM analysis in the 14Hf alloy consolidated by SPS (Diameter size = 2.0 ± 1.5 nm).

Fig. 9. 3D ion maps of 14Hf mechanically alloyed powder (Video 1)

Fig. 10. 3D ion maps from 3 different regions of the 14Hf alloy consolidated by SPS. Volume with a) no clusters (Video 2), b) volume with a low number density of clusters (Video 3) and c) volume with a high number density of clusters (Video 4).

Fig. 11. a) Cluster size (Guinier diameter) distribution for high and low cluster density regions (cluster size = 2.34 ± 0.77 and 3.64 ± 0.98, respectively) and b) cluster shape for high and low cluster density regions in the 14Hf alloy consolidated by SPS.

Fig. 12. O:Hf ratio as a function of the cluster size for for high and low cluster density regions in the 14Hf alloy consolidated by SPS.

Fig. 13. a) Nanoindentation hardness profiles for 14Hf as-milled powder and b) Vickers hardness measurements on 14Hf alloy consolidated by SPS.

Video captions

Video 1. 3D view of the ion maps displayed in Fig. 9 for the 14Hf mechanically alloyed powder.

Video 2. 3D view of the ion maps displayed in Fig. 10-a) for the volume with no clusters in the 14Hf alloy consolidated by SPS.

Video 3. 3D view of the ion maps displayed in Fig. 10-b) for the volume with a low number density of clusters in the 14Hf alloy consolidated by SPS.

Video 4. 3D view of the ion maps displayed in Fig. 10-c) for the volume with a high number density of clusters in the 14Hf alloy consolidated by SPS.

Highlights

- Fe-14Cr (wt.%) and pure Hf powders were mechanically alloyed and consolidated by SPS
- Microstructural and mechanical characterisation has been performed
- The ability of Hf to produce a dispersion of oxide nanoparticles is demonstrated

Table I

Table I. Chemical composition of the Fe-14Cr (wt. %) pre-alloyed powder

Element	Fe	Cr	Si	Mn	C	N	O
Wt. %	Bal.	14.13	0.281	0.194	0.004	0.0095	0.052

Table II

Table II. Summary of the cluster size, intercluster distance and number density of clusters in the 14Hf alloy consolidated by SPS in the low and high cluster density regions.

Alloy	Cluster size (nm)			Intercluster distance (nm)			Number density of clusters ($\times 10^{23}$ m^{-3})
	Range (nm)	Median (nm)	Mean value (nm)	Range (nm)	Median (nm)	Mean value (nm)	
Fe-14Cr-0.22Hf-SPS (low cluster density)	2.48-6.64	3.67	3.64 ± 0.98	6.63-26.59	16.86	17.81 ± 6.84	0.83
Fe-14Cr-0.22Hf-SPS (high cluster density)	0.78-3.82	2.26	2.34 ± 0.77	2.55-30.83	13.39	14.43 ± 7.81	2.37

Table III

Table III. Summary of the cluster shape in the regions with low and high number density of clusters in the14Hf alloy consolidated by SPS

Alloy	Cluster shape			
	Spherical	Disc shaped	Rod shaped	Lath shaped
Fe-14Cr-0.22Hf-SPS (low cluster density)	87%	0%	13%	0%
Fe-14Cr-0.22Hf-SPS (high cluster density)	84%	12%	4%	0%

Table IV

Table IV. Summary of hardness, total hardening, Orowan and Hall-Petch contributions to the total hardening for the 14Hf alloy consolidated by SPS and Fe-14Cr-0.3Y_2O_3 (wt.%) alloy consolidated by HIP [27, 45]. Hardness of Fe-14Cr consolidated by SPS is shown as the reference value [27].

Alloy	Hardness (GPa)	Total hardening (GPa)	Orowan hardening		Hall-Petch hardening	
			(GPa)	(%)	(GPa)	(%)
Fe-14Cr-SPS [27]	1.74 ± 0.04	- - - -	- - - -	- - - -	- - - -	- - - -
Fe-14Cr-0.3Y_2O_3-HIP [27, 45]	3.60 ± 0.08	1.86	1.11	59.5	0.75	40.5
Fe-14Cr-0.22Hf-SPS (this study)	2.31 ± 0.13	0.57	0.32	56.1	0.25	43.9

Table V

Table V. Orowan hardness calculations for the 14Hf alloy consolidated by SPS considering the different cluster density regions observed by APT.

Fe-14Cr-0.22Hf-SPS	Partial Orowan hardening (GPa)	Volume fraction (%)	Contribution to total Orowan hardening (GPa)
High cluster density region	0.329	35	0.115
Low cluster density region	0.749	27	0.202
No clusters region	0.000	38	0.000

Figure 1

Click here to download high resolution image

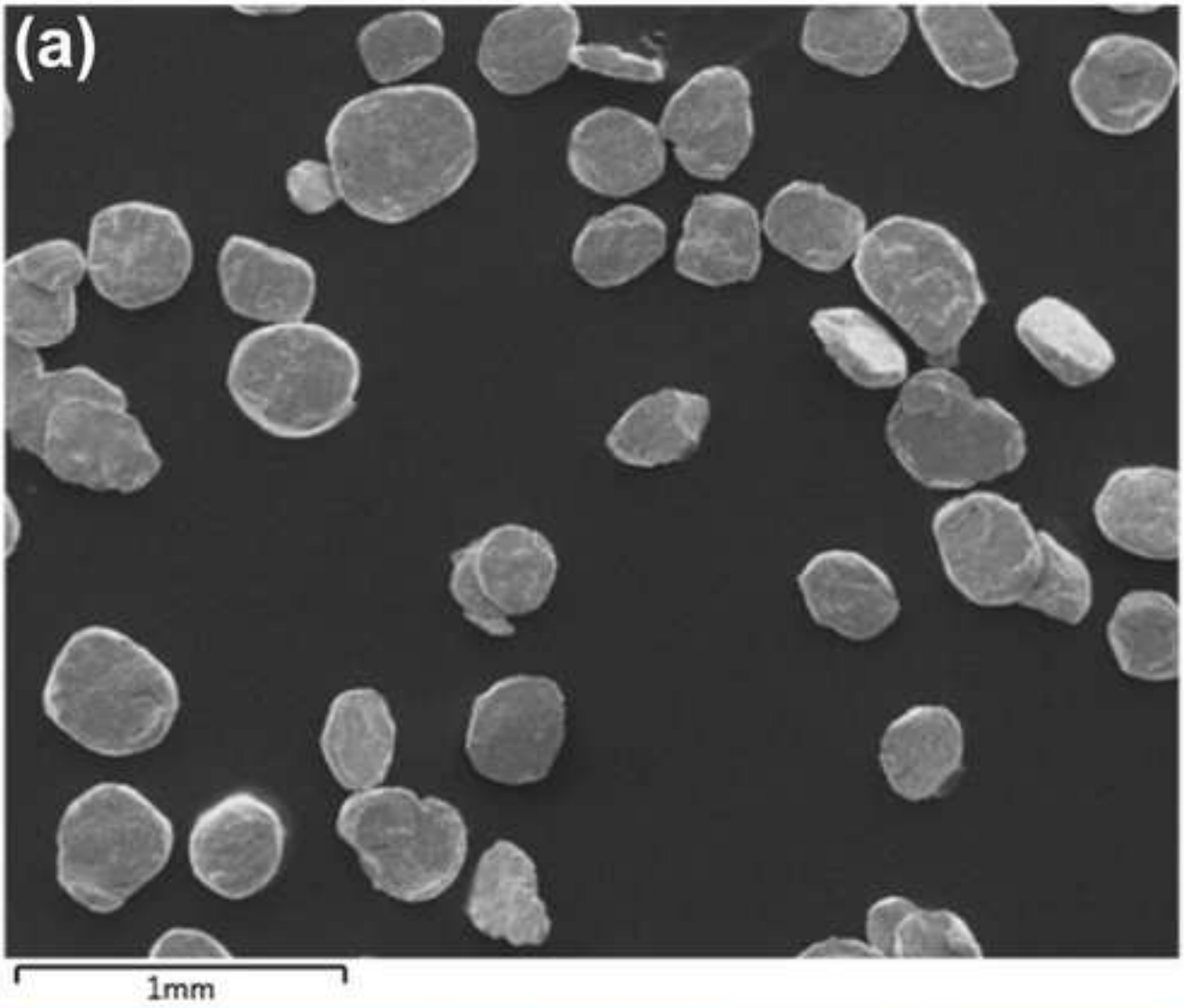

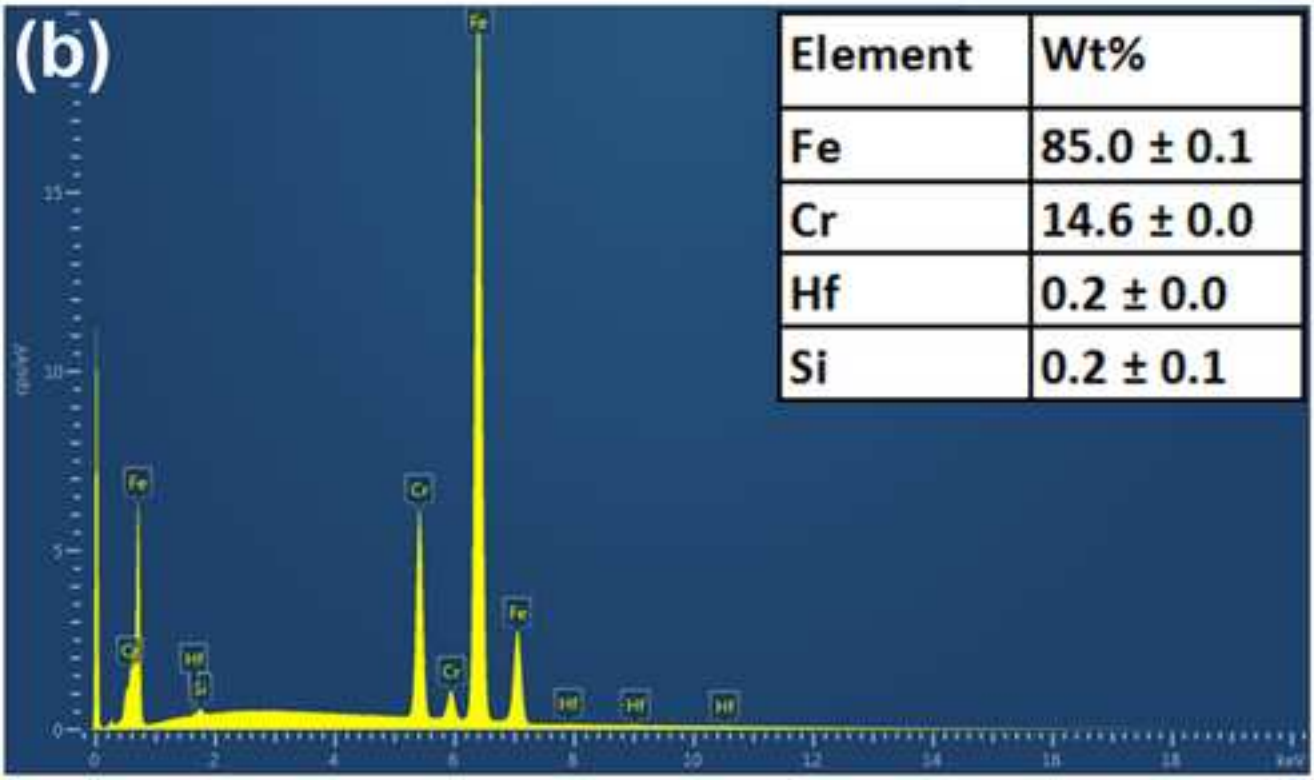

Element	Wt%
Fe	85.0 ± 0.1
Cr	14.6 ± 0.0
Hf	0.2 ± 0.0
Si	0.2 ± 0.1

Figure 2

Click here to download high resolution image

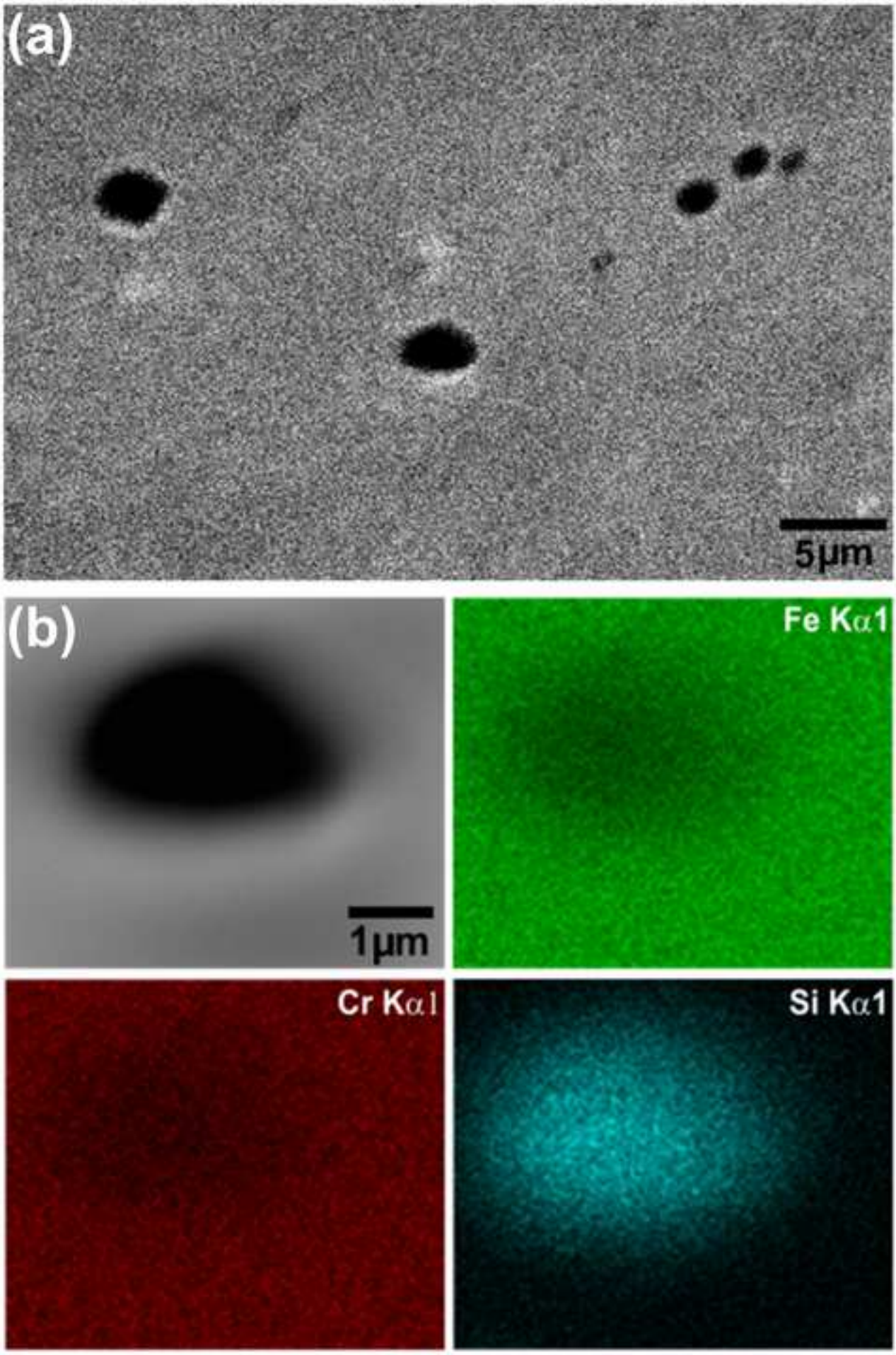

Figure 3
Click here to download high resolution image

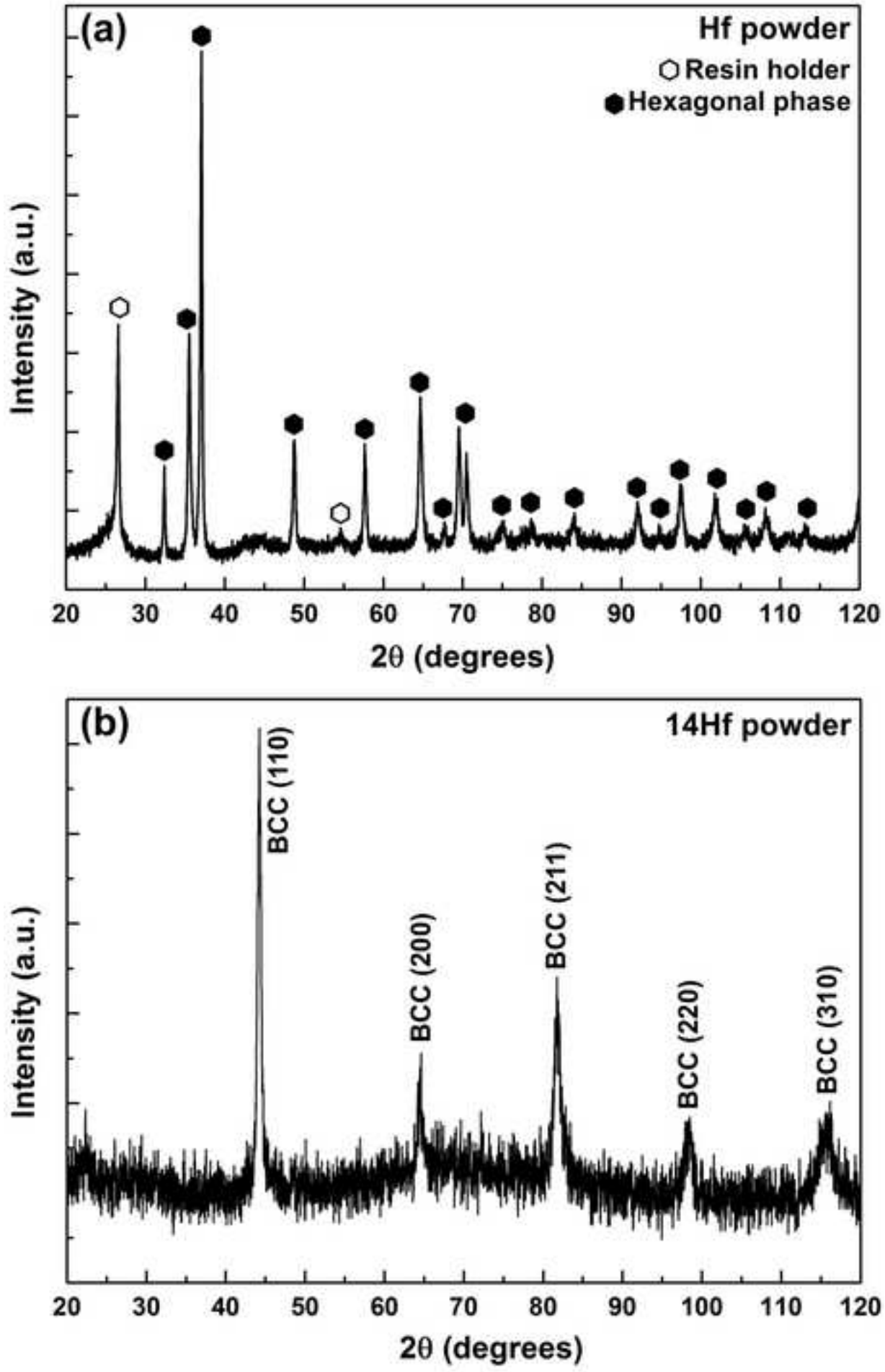

Figure 4

Click here to download high resolution image

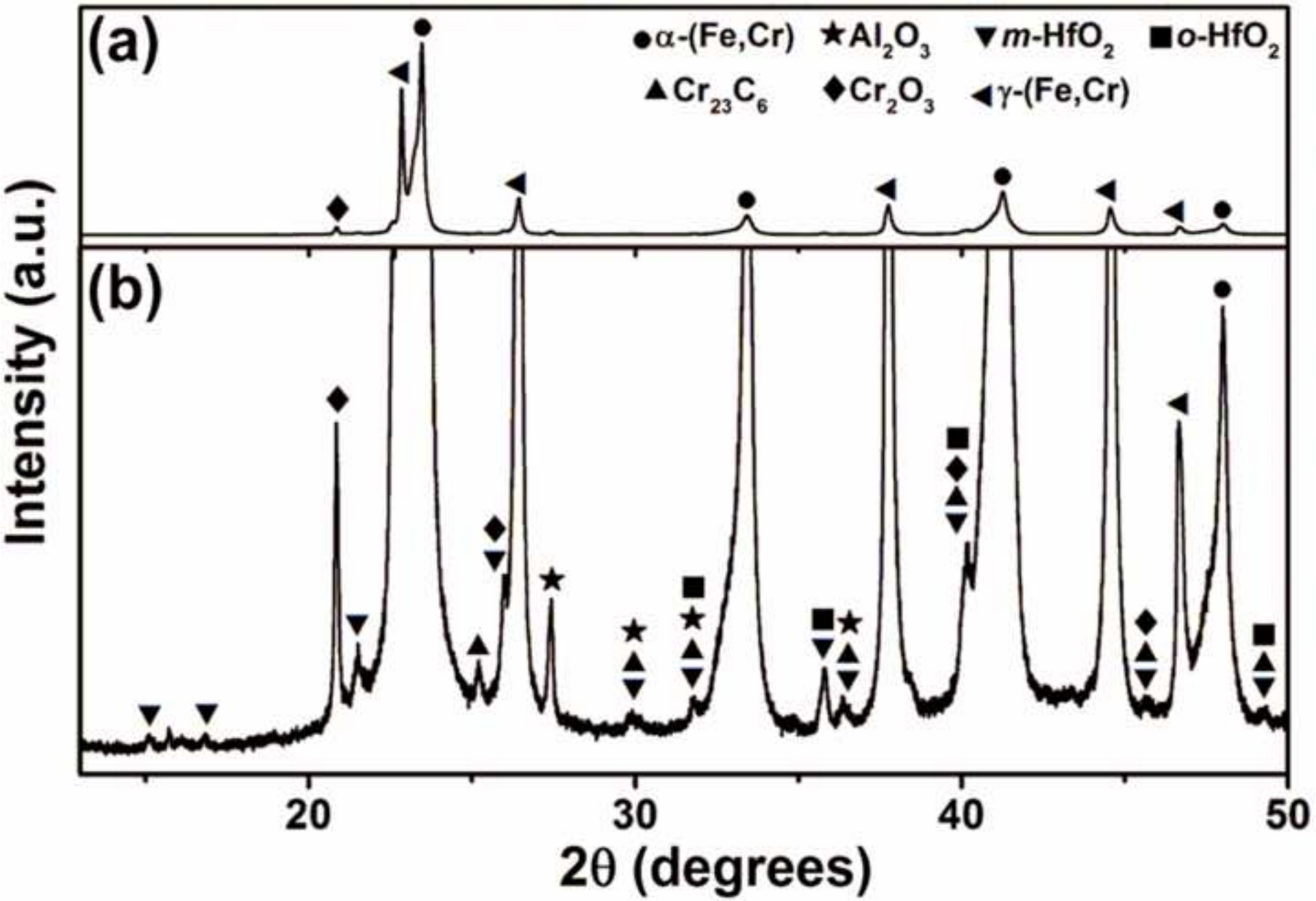

Figure 5

Click here to download high resolution image

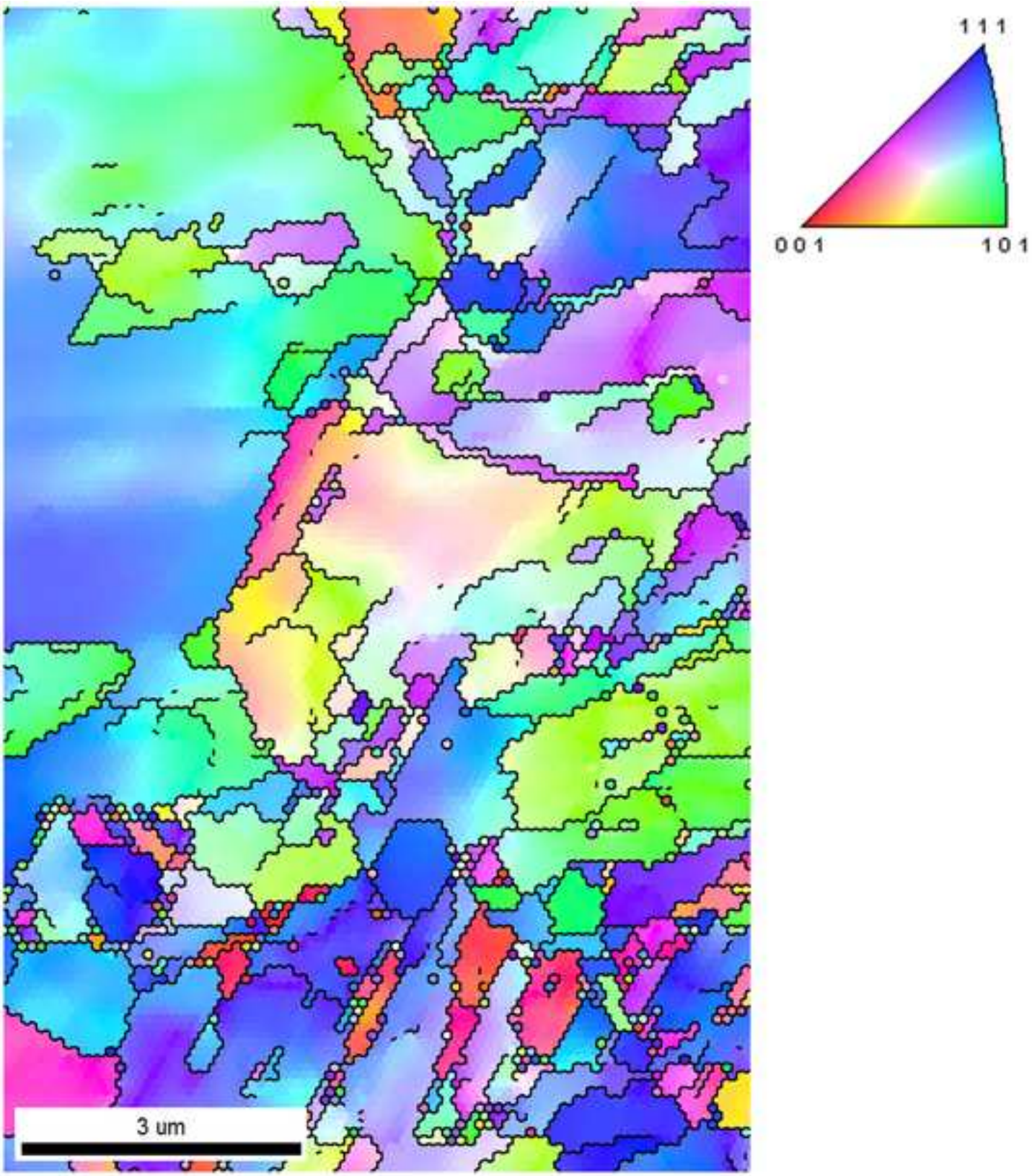

Figure 6

Click here to download high resolution image

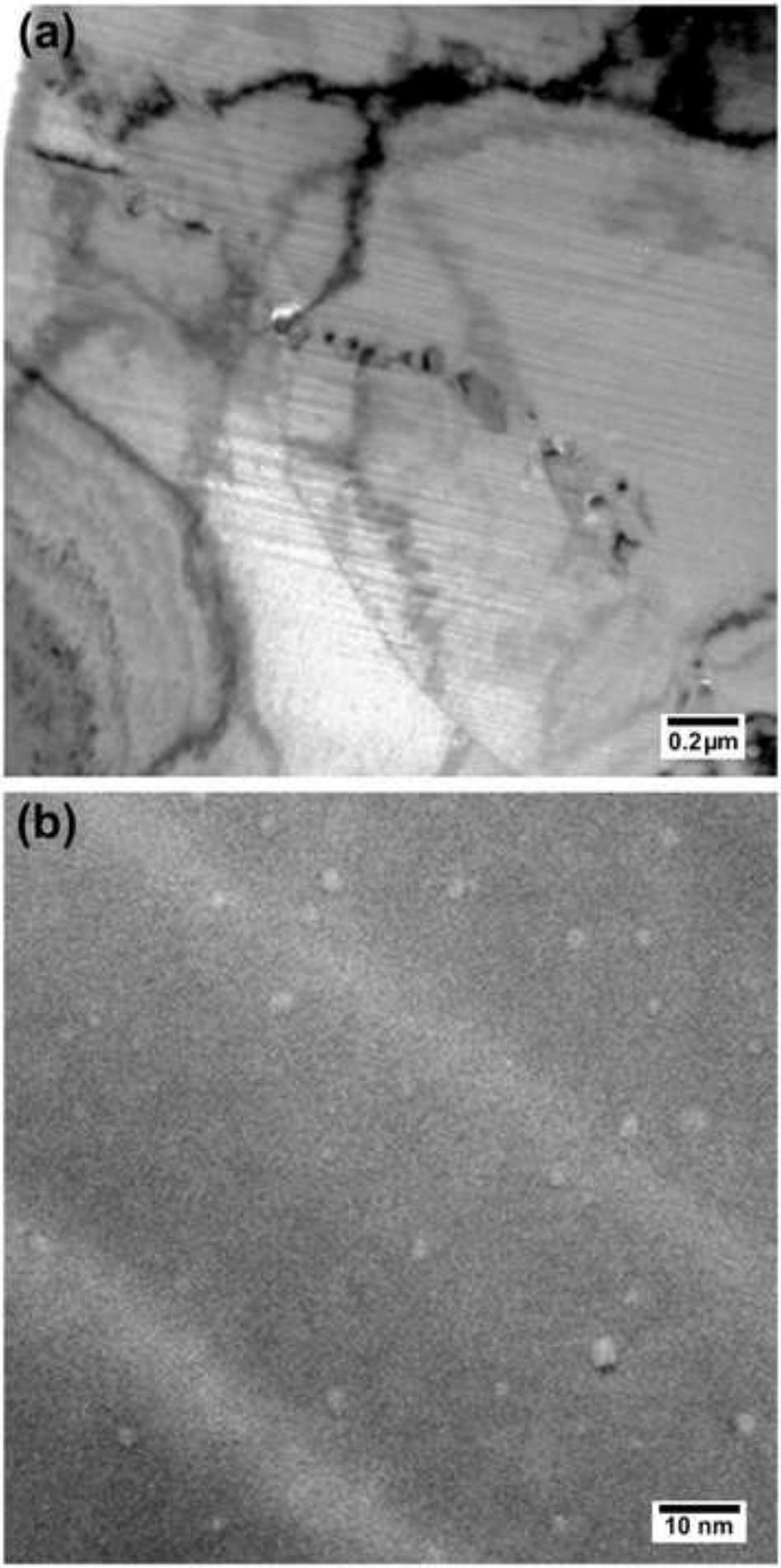

Figure 7

Click here to download high resolution image

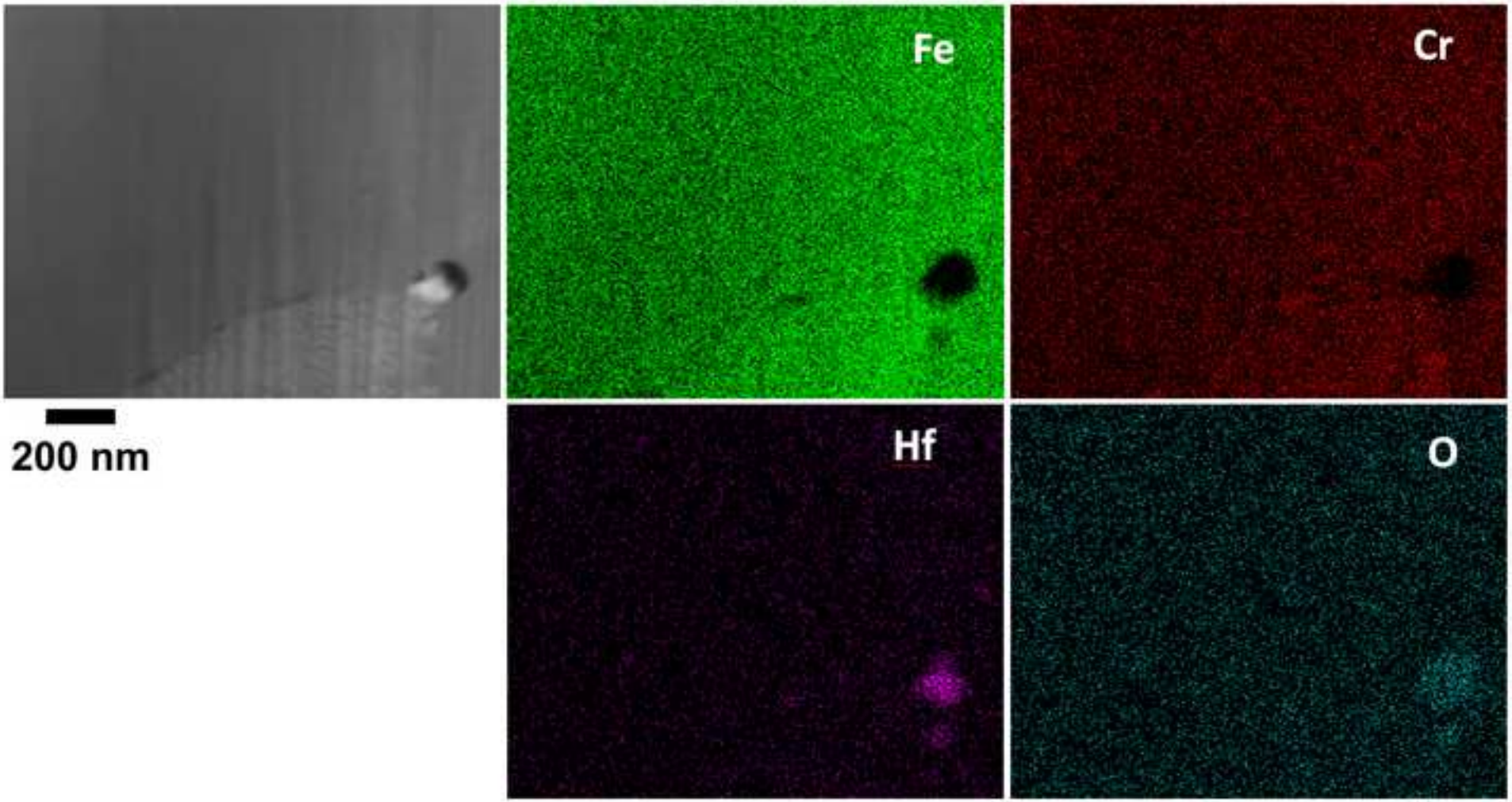

Figure 8

Click here to download high resolution image

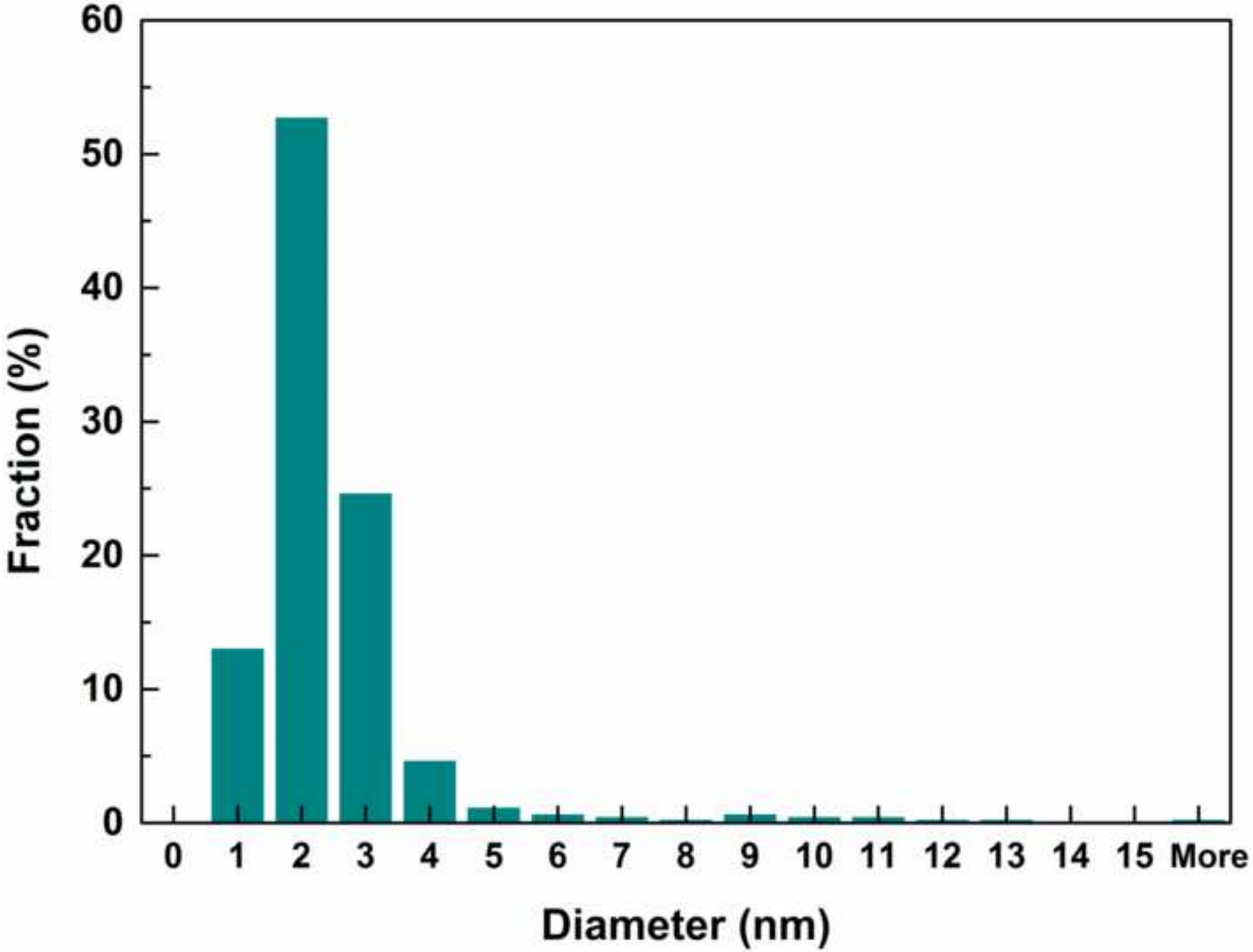

Figure 9

Click here to download high resolution image

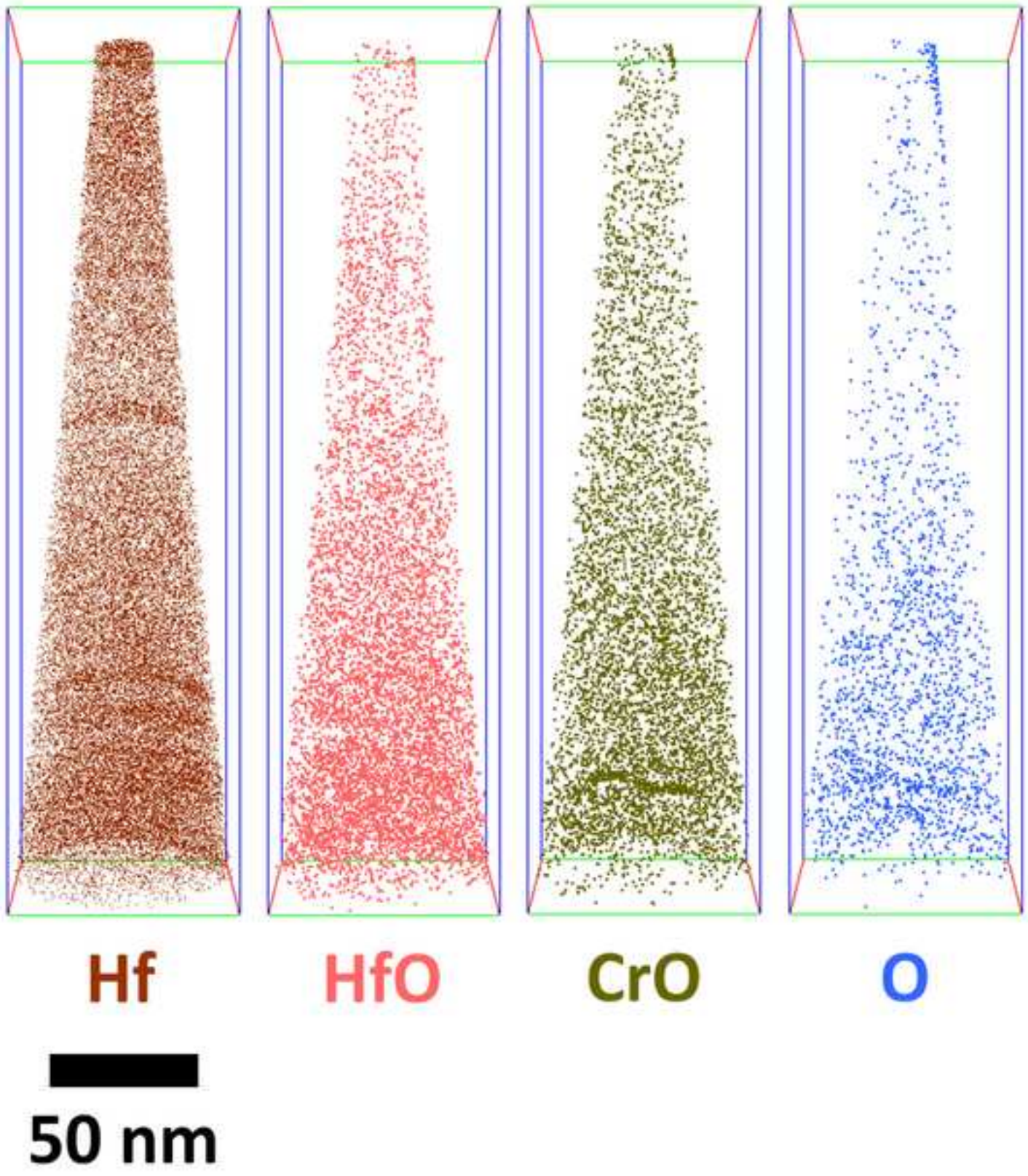

Figure 10

Click here to download high resolution image

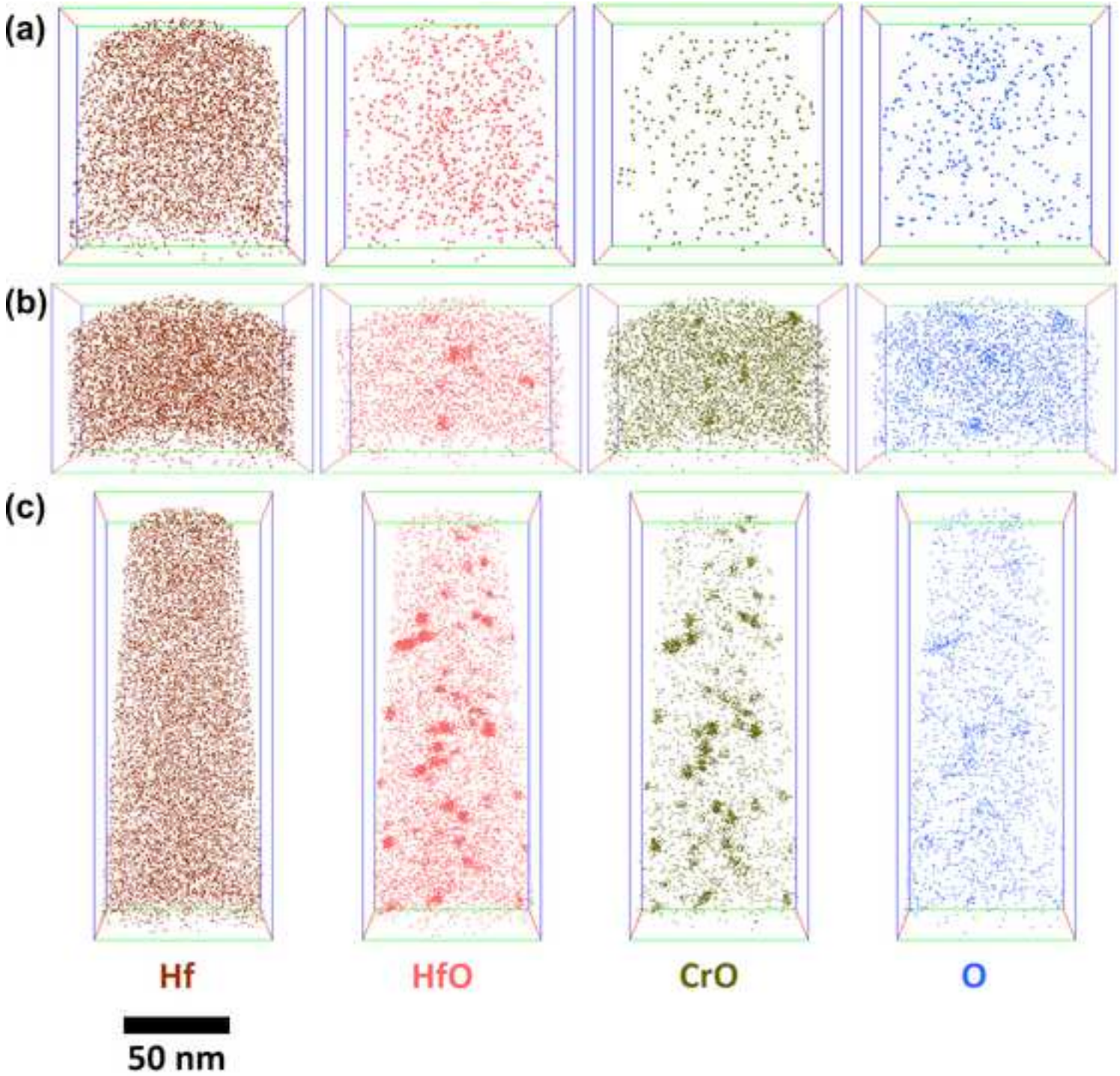

Figure 11

Click here to download high resolution image

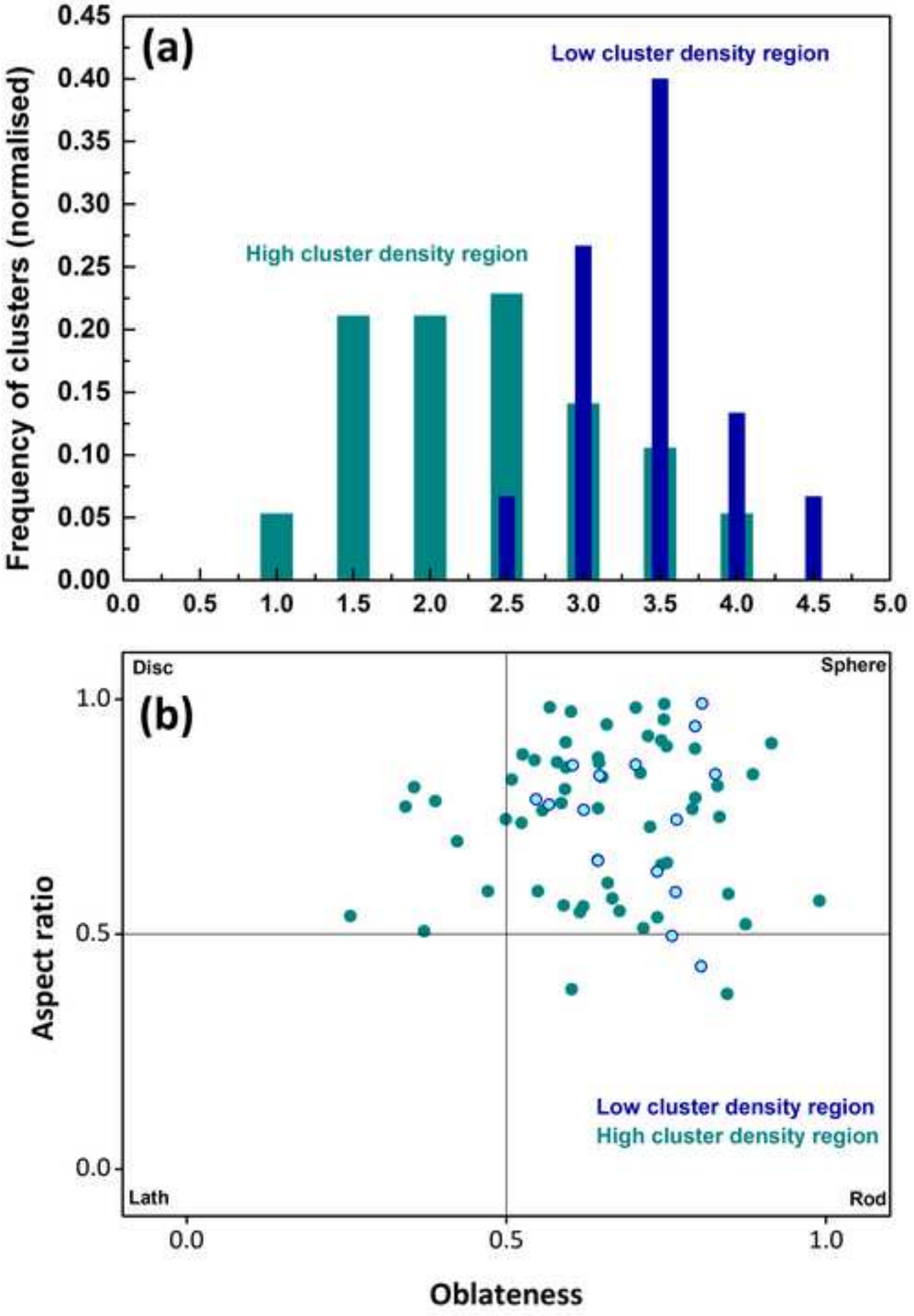

Figure 12

Click here to download high resolution image

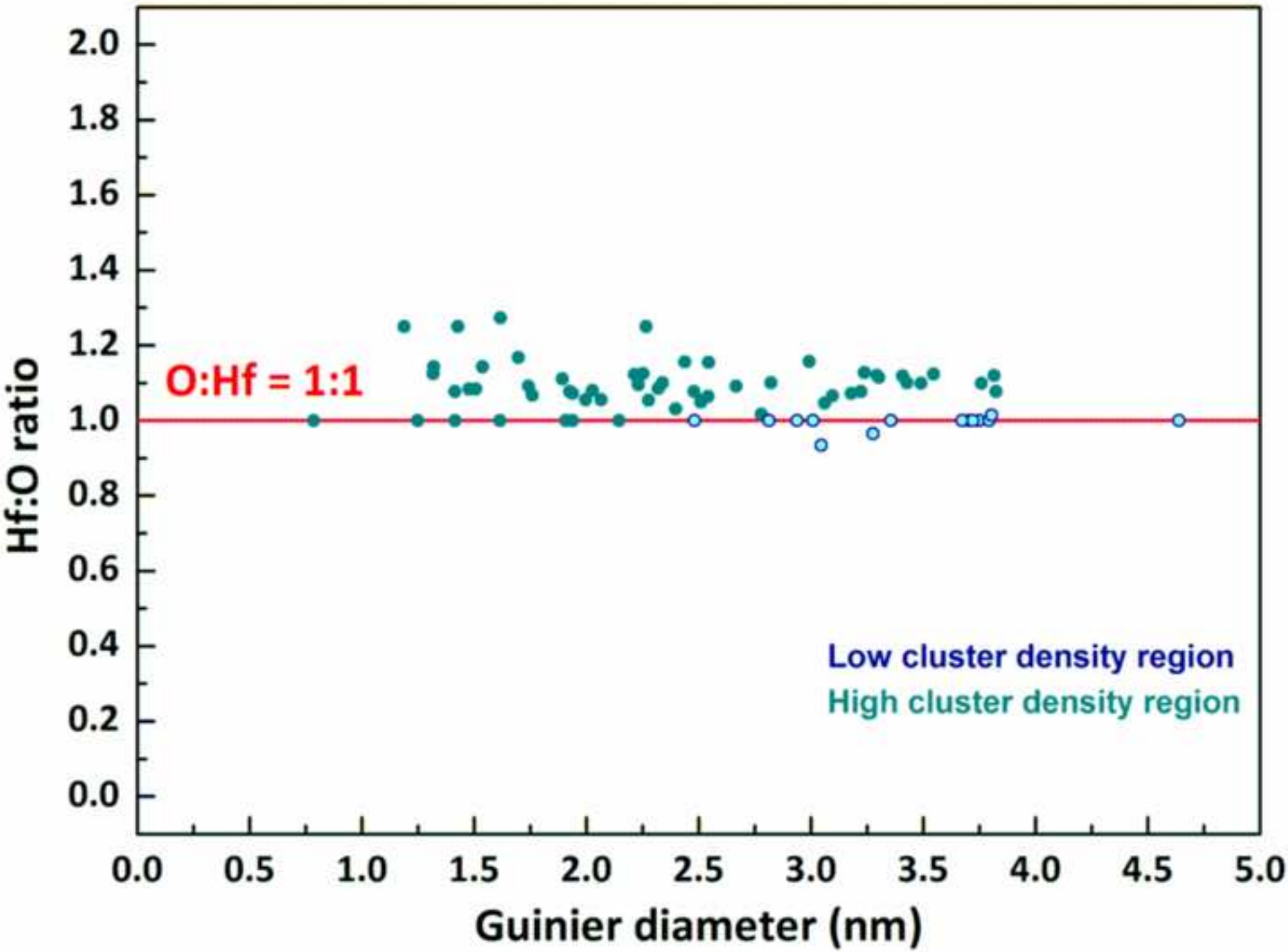

Figure 13
Click here to download high resolution image

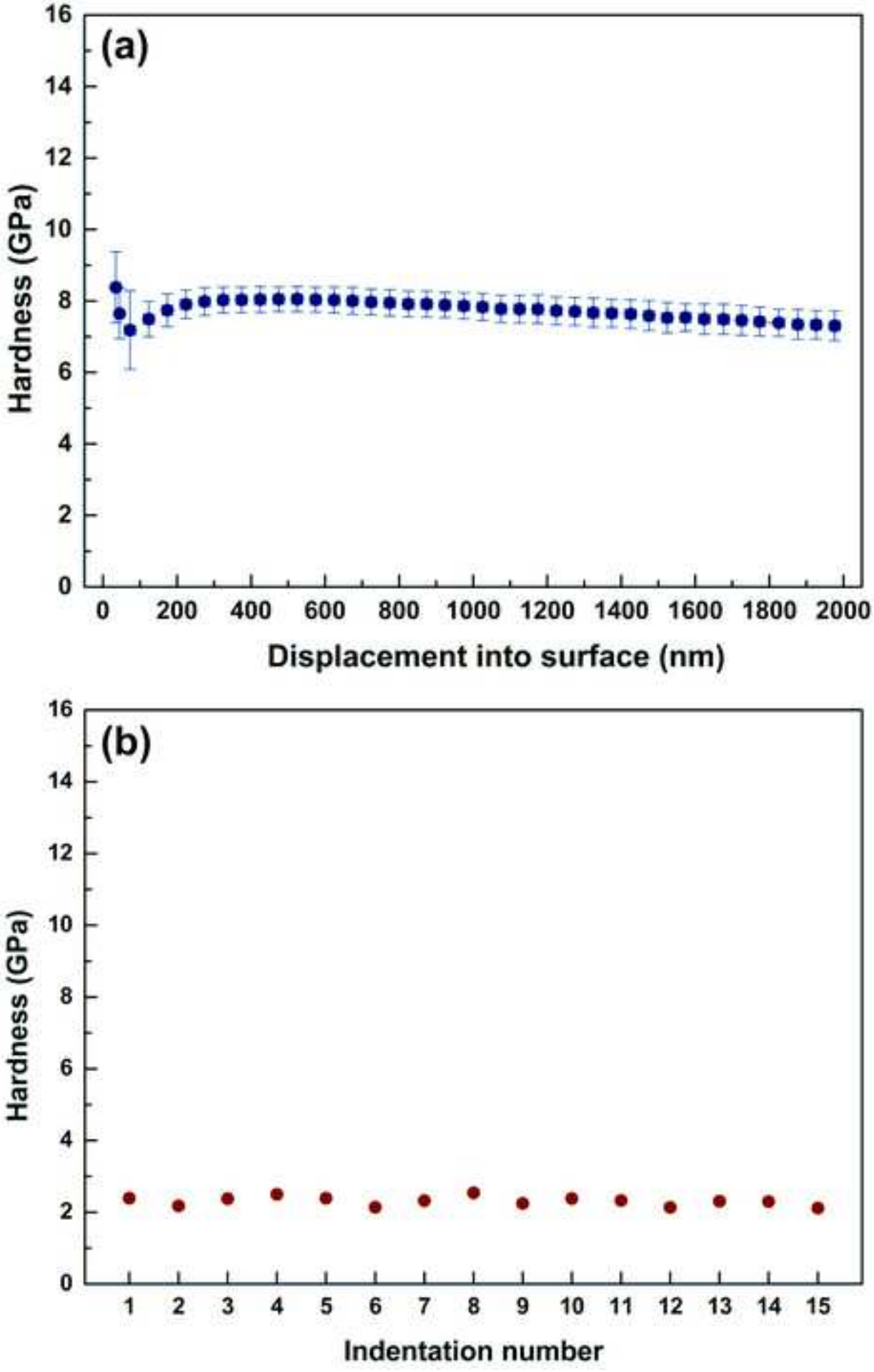

Video 1

Click here to download Supplementary Material for on-line publication only: JALCOM_APT-Fig_9.mp4

Video 2

Click here to download Supplementary Material for on-line publication only: JALCOM_APT-Fig10a.mp4

Video 3

Click here to download Supplementary Material for on-line publication only: JALCOM_APT-Fig10b.mp4

Video 4

Click here to download Supplementary Material for on-line publication only: JALCOM_APT-Fig10c.mp4